

Recyclable nanocomposites of well-dispersed 2D layered silicates in  
cellulose nanofibril (CNF) matrix

*Original*

Recyclable nanocomposites of well-dispersed 2D layered silicates in  
cellulose nanofibril (CNF) matrix / Li, Lengwan; Maddalena, Lorenza; Nishiyama, Yoshiharu; Carosio, Federico; Ogawa,  
Yu; Berglund, Lars. - In: CARBOHYDRATE POLYMERS. - ISSN 0144-8617. - ELETTRONICO. - 279:(2022).  
[10.1016/j.carbpol.2021.119004]

*Availability:*

This version is available at: 11583/2971337 since: 2022-09-16T07:54:16Z

*Publisher:*

Elsevier

*Published*

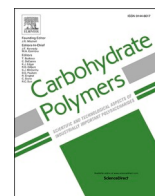
DOI:10.1016/j.carbpol.2021.119004

*Terms of use:*

This article is made available under terms and conditions as specified in the corresponding bibliographic description in  
the repository

*Publisher copyright*

(Article begins on next page)



## Recyclable nanocomposites of well-dispersed 2D layered silicates in cellulose nanofibril (CNF) matrix

Lengwan Li<sup>a</sup>, Lorenza Maddalena<sup>b</sup>, Yoshiharu Nishiyama<sup>c</sup>, Federico Carosio<sup>b</sup>, Yu Ogawa<sup>c</sup>, Lars A. Berglund<sup>a,\*</sup>

<sup>a</sup> Department of Fiber and Polymer Technology, Wallenberg Wood Science Center, KTH Royal Institute of Technology, 10044 Stockholm, Sweden

<sup>b</sup> Dipartimento di Scienza Applicata e Tecnologia, Politecnico di Torino, Alessandria Campus, Viale Teresa Michel 5, 15121 Alessandria, Italy

<sup>c</sup> Univ. Grenoble Alpes, CNRS, CERMAV, 38000 Grenoble, France

### ARTICLE INFO

#### Keywords:

Nanocellulose fibrils  
Biocomposites  
Sustainable  
Mechanical properties  
Wide-angle X-ray diffraction

### ABSTRACT

Nanocomposites based on components from nature, which can be recycled are of great interest in new materials for sustainable development. The range of properties of nacre-inspired hybrids of 1D cellulose and 2D clay platelets are investigated in nanocomposites with improved nanoparticle dispersion in the starting hydrocolloid mixture. Films with a wide range of compositions are prepared by capillary force assisted physical assembly (vacuum-assisted filtration) of TEMPO-oxidized cellulose nanofibers (TOCN) reinforced by exfoliated nanoclays of three different aspect ratios: saponite, montmorillonite and mica. X-ray diffraction and transmission electron micrographs show almost monolayer dispersion of saponite and montmorillonite and high orientation parallel to the film surface. Films exhibit ultimate strength up to 573 MPa. Young's modulus exceeds 38 GPa even at high MTM contents (40–80 vol%). Optical transmittance, UV-shielding, thermal shielding and fire-retardant properties are measured, found to be very good and are sensitive to the 2D nanoplatelet dispersion.

### 1. Introduction

This study explores eco-friendly nanocomposites and the potential to improve dispersion and orientation of 2D layered anionic clays in a non-porous matrix of 1D flexible cellulose nanofibrils (CNF). Developments of the colloidal suspensions results in excellent mechanical properties and high optical transmittance even at very high clay content. The nanocomposites are readily recycled, demonstrating high performance and multifunctionality in combination with eco-friendly attributes.

Polymer matrix nanocomposites can have strongly improved physical properties, due to effects from small amounts of hard reinforcing nanoparticles (Kojima et al., 1993; Mianehrow et al., 2020). At high volume fraction of nanoparticles, however, problems with nanoparticle agglomeration leads to decreased mechanical properties (Dzenis, 2008). Two-dimensional (2D) platelets (bricks) offer possibilities when combined with polymer matrix (mortar) to form high volume fraction brick-and-mortar composites (Benítez & Walther, 2017; Liu, Cottrill, et al., 2018). At least theoretically, the volume fraction of 2D platelets can be very high in such composites. The classical example is nacre, where the fraction of oriented inorganic platelets may exceed 90 vol%, with an

organic chitin/protein mixture serving as polymeric binder (Liu & Jiang, 2011). Kotov and coworkers used layer-by-layer adsorption (LbL)-techniques to create well-ordered nanocomposites in the form of nacre-mimetic, thin films of very high mechanical properties (Yang et al., 2012). They were composed of clay nanoplatelets (montmorillonite, MTM) and water-soluble polymer matrices such as polyelectrolytes (Tang et al., 2003) or polyvinyl alcohol (PVA) (Podsiadlo et al., 2007). Grunlan et al. used a similar concept to show that thin coatings with nacre-like structure were able to provide fire retardancy to textile fibers (Carosio et al., 2011; Li et al., 2010) and cellular foams (Kim et al., 2011), and gas barrier properties to plastic bottles (Laufer et al., 2012). Jiang et al. designed ternary nacre-inspired films based on MTM/PVA/cellulose nanofibrils (CNF) by liquid casting (Wang, Cheng, et al., 2014), but the Young's modulus were below 25 GPa, substantially lower than reported here.

Clay platelets are crystalline in two-dimensions, have high strength and in-plane modulus (Yang et al., 2012) with significant structural anisotropy. They are naturally occurring, in the form of abundant stacked nanosheets available in the soil as mineral deposits. Replacement of man-made material components by clay platelets can therefore

\* Corresponding author.

E-mail address: [blund@kth.se](mailto:blund@kth.se) (L.A. Berglund).

<https://doi.org/10.1016/j.carbpol.2021.119004>

Received 20 September 2021; Received in revised form 1 November 2021; Accepted 7 December 2021

Available online 14 December 2021

0144-8617/© 2022 The Authors. Published by Elsevier Ltd. This is an open access article under the CC BY license (<http://creativecommons.org/licenses/by/4.0/>).

contribute to sustainable development, which is more challenging for many other nanoparticles and nanomaterials. Sustainability problems can arise from toxicity, high processing energy demands, high global warming potential and lack of recycling options. Clay nanocomposites should also be combined with bio-based polymer matrices. In the present study, CNF nanofibers form the matrix phase, the “mortar”. The neat random-in-plane CNF films can reach a modulus as high as 25 GPa (Yang et al., 2021). TEMPO-oxidized CNF is a specific type of CNF nanofiber, often termed TOCN (Y.R.I. Ltd., 2018), which is used in the present investigation. TOCNs are commercially available in Japan. TOCNs are flexible fibrils, typically  $\approx 4$  nm in diameter, more than 700 nm in length, with carboxyl groups on the fibril surface (Saito et al., 2006; Saito et al., 2007). They have excellent mechanical properties (Saito et al., 2013; Šturcová et al., 2005; Tanpichai et al., 2012; Wohler et al., 2012) and due to the high density of negative surface charge, they are readily dispersed in the form of stable hydrocolloids. Oriented nanocellulose films can also be prepared based on TOCN (Li et al., 2021).

The first investigations of CNF/clay nanocomposites were based on scalable vacuum filtration and drying of native CNF dispersed as colloidal mixtures with MTM nanoclay platelets (Liu et al., 2011; Sehaqui et al., 2010). In a later patent, application examples included paper and packaging board coatings, printed electronic substrates and barrier layers, for instance gas barrier layers replacing aluminium films in liquid packaging (Berglund, 2014). Isogai and coworkers reported on CNF/saponite (SPN, aspect ratio  $\sim 50$ ) (Wu et al., 2014) and CNF/MTM (Wu et al., 2012) thin films ( $< 10$   $\mu\text{m}$ ) prepared by slower solution casting resulting in very high tensile strength (over 500 MPa) obtained at low clay content. Liimatainen et al. made CNF/talc hybrid films of fairly high strength (211 MPa) with interesting oxygen barrier properties (less than 0.001  $\text{cm}^3\cdot\text{mm}/\text{m}^2\cdot\text{day}$ ) (Liimatainen et al., 2013). Carosio et al. reported on halogen-free CNF/MTM films with exceptionally good thermal shielding ( $< 0.08$   $\text{W}\cdot\text{m}^{-1}\cdot\text{K}^{-1}$ ) and fire-retardancy properties (Carosio et al., 2015; Carosio et al., 2016). There is a technology (Husband et al., 2015) in industrial use, where co-grinding of pulp fibers and high aspect ratio clays (e.g. kaolinite) results in a material containing nanoscale particles, although the average structure is much coarser than in the present study. These studies, however, did not investigate effects of dispersion and clay aspect ratio on properties.

In order to fully realize the potential of polymer matrix 2D nanocomposites, high reinforcement content should be combined with well-dispersed nanoscale particles. Zhao et al. (2020) reports exceptional mechanical properties for high reinforcement content thin films ( $\approx 1$   $\mu\text{m}$ ) composed of well-oriented graphene oxide or clay sheets combined with carbon nanotubes and PVA. Although this is an interesting result, film formation in the thickness range of 30–100  $\mu\text{m}$  would be necessary to extend practical processing from colloids to multifunctional films, coatings and laminates. In an excellent review (George & Ishida, 2018) of high volume fraction nanocomposites, Ishida points out the need for scalable processing methods suitable for such materials, and the need to combine strength and toughness. Other 2D nanoplatelets could be used with the present approach, including the possibility to make “architectured” nanocomposite laminates (Nepal et al., 2021).

It is hypothesized that vacuum-assisted filtration of high aspect ratio and well-dispersed nanoparticle in CNF matrix can lead to high-performance CNF/clay nanocomposite of around 30  $\mu\text{m}$  in thickness, of interest for coatings, films and laminates contributing to sustainable development. A wide range of compositions are investigated, as well as clay platelets of different aspect ratio (montmorillonite, saponite and mica). High 2D platelet content is also investigated, since modulus only increased up to 35 vol% in a previous investigation (Medina, Nishiyama, et al., 2019). Particular care was taken to ensure good 2D nanoparticle dispersion, combined with extensive characterization of nanostructural effects. Remarkable ultimate tensile strength (573 MPa) and the highest reported Young's modulus (over 50 GPa) for TOCN/MTM were obtained, and the properties were better than previous studies at very high MTM

contents. These properties were combined with UV-shielding, thermal shielding and fire retardancy without the use of halogens. The possibility for recycling was also investigated, since the film is assembled by reversible secondary bonds. Characterization tools include transmission electron microscopy (TEM), X-ray diffraction and solid state nuclear magnetic resonance spectroscopy (SS-NMR) for quantification of clay size, orientation, dispersion and agglomeration state. Critical nanostructural parameters are discussed to clarify clay reinforcement mechanisms and related functionalities.

## 2. Experimental section

### 2.1. CNF preparation

The CNF suspension was prepared by using TEMPO-oxidation developed by Saito et al. Bleached softwood sulfite pulp fibers provided by Nordic Paper Seffle AB, Säffle, Sweden with 14 wt% hemicellulose and  $< 1\%$  lignin. The pulp (20 g by dry weight) was demineralized by stirring in a diluted HCl solution at pH 2.5 for 2 h, followed by washing with DI water by filtration. Then, the pulp was suspended in distilled water (2000 mL) containing TEMPO (0.32 g) and NaBr (2 g). A 1.8 M NaClO (60 mL) was slowly dropped to the suspension and the pH of suspension was maintained at 11 by adding NaOH. After 1 h, the oxidized pulp was washed by DI water. The oxidized pulp was further treated with 1% NaClO<sub>2</sub> in an acetate buffer at pH 4.8 for 24 h. The oxidized pulp had a carboxylate content of  $\sim 1$  mmol/g. After washing, the pulp fibers passed through a high pressure microfluidizer (Microfluidizer M-110EH, Microfluidics Corp, Newton, Massachusetts, USA) once in 200  $\mu\text{m}$  channels and twice in 100  $\mu\text{m}$  channels to achieve transparent TEMPO-CNF colloid (0.82 wt%). The TEMPO CNF (TOCN) was diluted to 0.1 wt% for zeta potential measurement, the value is  $-121$  mV.

### 2.2. Clay dispersion

Synthetic saponite (SPN) and natural montmorillonite (MTM) were supplied by Kunimine Industries, with a density of 2.86  $\text{g}/\text{cm}^3$ . The MTM and SPN dispersions were prepared using the same approach. A small amount of powders (1 wt%) were added into deionized water and shear mixed by using an Ultra-turrax for 10 min. The dispersion was then sonicated 5 min (750 W for 0.6 L dispersion) and subsequently centrifugation 30 min at 4500 rpm. The supernatant phase was kept for next sonication cycles, while the aggregation in the bottom of the tube was removed. Sonication/centrifugation cycles were repeated three times. The concentration of the stable dispersion was measured to be around 0.65 wt%. Sericite mica with 1250 mesh, a density of 2.65  $\text{g}/\text{cm}^3$  were given by Huayuan Mica Co., Ltd. The mica dispersion (1 wt%) was shear mixed by Ultra-turrax in deionized water then let the aggregates sediment for 16 h and obtained the dispersion ( $\sim 0.3$  wt%).

### 2.3. Nanopaper preparation

Clay dispersions were slowly added into TOCN water dispersion and sheared by an Ultra-turrax apparatus with a speed set at 12,000 rpm. The final concentration of TOCN/clay mixture dispersion was controlled to be around 0.1 wt%. The shear-mix process was maintained for 2–5 min until the speed of Ultra-turrax became stable, which indicates the co-dispersions were well mixed and has relatively constant viscosity. The co-dispersions were then vacuum filtered by using the assembly with fritted glass setup and PVDF hydrophilic membrane filter with a pore size of 0.65  $\mu\text{m}$ . Filtration time is about 16 h for the TOCN and TOCN/SPN colloids, whereas it is longer for TOCN/MTM due to larger platelets, and filtration time increases with MTM content. The TOCN/40%MTM (C40%MTM) sample has the longest filtration time ( $\sim 48$  h), possibly because of good MTM dispersion combined with high MTM content. The obtained wet cakes were put between PVDF membranes

and then sandwiched by woven metal cloths. This package was placed in a Rapid-Köthen dryer for 15 min at 93 °C under vacuum condition. The vacuum pressure was reduced for high mica content samples. For brevity, the sample name of TOCN/clay nanocomposites films are abbreviated, such as C20%SPN (TOCN/20 vol% SPN), C40%MTM (TOCN/40 vol% MTM).

## 2.4. Nanopaper recycling process

Nanopaper films were torn into pieces (~1 cm) and then sheared by an Ultra-turrax in water for about 5 min. Next, the dispersions were kept at room temperature for ~24 h before shearing by Ultra-turrax again for 5 min. The dispersions were then made into nanopaper film again following the procedure described above. Four rounds of recycling were carried out in total, and the nanopapers were termed accordingly from 0 to 4.

## 2.5. Characterizations

### 2.5.1. Atomic force microscopy

Atomic force microscopy was carried out using a Bruker Multimode 8. The AFM was operated in the ScanAsyst mode with cantilevers having a nominal tip radius of 2 nm and a spring constant of 0.4 N/m. Prior to the test, silicon wafers were rinsed with water and was plasma treated for 2 min, then it was immersed in 0.1 wt% polyethylenimine solution for 10 min. After raising with DI water and drying it was immersed in TOCN and TOCN/clay dispersion (0.1 g/L) for 10 min and left to dry after rinsing with DI water.

### 2.5.2. Transmission electron microscopy

The TOCN/clay composites were first cross-linked by soaking the composite films in 1% glutaraldehyde aqueous solution for 1 h, followed by water rinsing and EtOH series dehydration. The dehydrated samples were embedded in an epoxy resin. The transverse ultrathin sections of embedded films were prepared using an Ultracut UC6 microtome (Leica Microsystems, Austria) with a 35-degree diamond knife (DiATOME, USA). The sections with a thickness of ca. 90 nm were collected on glow-discharged carbon coated copper grids. The samples were then observed using a transmission electron microscopy JEM-2100Plus (JEOL Ltd., Japan), operated at an accelerating voltage of 200 kV. The electron micrographs were recorded using a Gatan Rio 16 camera (Gatan Inc., USA). A tilt series acquisition was performed using SerialEM (Mastrorarde, 2003) between tilt angles of  $\pm 60^\circ$  with an angle increment of  $2^\circ$ . The image alignment and 3D reconstruction were done using IMOD software suit. The reconstructed tomogram was visualized using 3dmod.

### 2.5.3. Scanning electron microscopy

The fractured cross section of samples after tensile testing was observed with a Hitachi S-4800 field emission scanning electron microscope (FE-SEM, Hitachi, Japan). Samples were coated with a thin Pd/Pt layer prior to observation. The typical operating conditions were ~8 mm working distance and 1 kV accelerating voltage. Energy-dispersive X-ray spectroscopy (EDX) was used for elemental analysis with an accelerating voltage of 15 kV during sample examination. The working distance was 15 mm. The morphology of post combustion residues collected from flame test was investigated using EVO15 (Zeiss, Germany) scanning electron microscope (beam voltage 20 kV). The samples were positioned on conductive tape and were mounted showing in cross section the most exposed surface to the flame. Observation was conducted in variable pressure (or low vacuum mode) in order to avoid super-exposition.

### 2.5.4. Tensile testing

The TOCN/clay nanocomposites films with a thickness around 30  $\mu\text{m}$  were cut into a 70 mm by 5 mm rectangle. The samples were cut by a LEICA Microtome blade after being conditioned in a  $50 \pm 2\%$  relative

humidity (R.H.) and  $22 \pm 1$  °C room for at least 2 days. The films were tested by a Universal Testing Machine (Instron 5944, USA) equipped with a 500 N load cell and a video extensometer. The span length was set to 25 mm and the crosshead speed was 2.5mm/min. All samples were tested more than 5 times. The modulus was determined by fitting a linear curve from the initial elastic region.

### 2.5.5. UV-vis

Ultra violet-visible spectra of TOCN/clay suspensions was measured by a UV-2550 Shimadzu spectrophotometer with an integrated sphere, the collecting range was from 200 to 800 nm with 0.5 nm interval. Haze measurements of films were carried out according to the ASTM D1003 standard which we described in detail previously (Medina, Nishiyama, et al., 2019).

### 2.5.6. Zeta potential

The Zetasizer ZEN3600 instrument from Malvern Instruments was utilized for charge determination of TOCN and clay dispersions in water with the concentration of ~0.5 wt% at pH = 6. Each sample was measured three times. Normally, Zeta potential greater than  $\pm 61$  mV indicates excellent stability, between  $\pm 40$  to  $\pm 60$  mV means good stability while  $\pm 30$  to  $\pm 40$  mV suggests moderate stability (Kumar & Dixit, 2017).

### 2.5.7. Total charge determination

The total carboxylate content of TEMPO-oxidized pulp fibers was determined by conductometric titration (standard method SCAN-CM 65:02). In short, pulp fibers were soaking in 0.1 M HCl for ~1 h to transfer to proton form and then washed by deionized water until a conductivity below 5  $\mu\text{S}/\text{cm}$  reached. After that, pulp fibers were titrated with NaOH, the carboxylate content can be calculated based on the consumption of NaOH.

### 2.5.8. Total porosity

We calculated the porosity based on

$$\text{Total porosity} = 1 - \rho^* / \rho_s \quad (1)$$

where  $\rho^*$  is the measured bulk density and  $\rho_s$  is the theoretical composite density, assuming 1.6  $\text{g}/\text{cm}^3$  for neat TOCN, 2.86  $\text{g}/\text{cm}^3$  for SPN and MTM, and 2.65  $\text{g}/\text{cm}^3$  for mica.

### 2.5.9. Wide-angle X-ray diffraction

Wide-Angle X-ray Diffraction measurement (WAXD) were performed on a point collimated Anton Paar's SAXSpoint 2.0 system (Anton Paar, Graz, Austria) equipped with a Microfocus X-ray source (Cu  $K\alpha$  radiation, wavelength 1.5418 Å) and an Eiger R 1M Tilt detector with  $75 \times 75$   $\mu\text{m}$  pixel size. All measurements were performed with a beam size of approximately 500  $\mu\text{m}$ , at room temperature with a beam path pressure at about 1–2 mbar. The sample to detector distance was set to 77 mm. All samples were mounted with the beam parallel to the film surface inside the vacuum chamber, and exposed for 10 min. The data reduction was performed by using SAXSanalysis software (Anton Paar, Graz, Austria).

### 2.5.10. Solid-state nuclear magnetic resonance spectroscopy

$^{13}\text{C}$  cross polarization/magic angle spinning (CP/MAS) nuclear magnetic resonance (NMR) spectra of the composite and the TOCN neat films were measured with a Bruker Avance II spectrometer operating at 100 MHz for  $^{13}\text{C}$ . The dry samples were packed in a zirconia rotor with a diameter of 3 mm. The measurement was performed with a spinning speed of 12 kHz, a sweep width of 29,761 Hz, a recycle delay of 2 s and a cross-polarization contact of 2 ms. The  $^{13}\text{C}$  chemical shifts were calibrated with the glycine carboxyl group at 176.03 ppm.

### 2.5.11. Fire retardancy

The flammability of prepared samples has been tested in horizontal

and vertical configurations; the sample ( $60 \times 15 \times 0.03 \text{ mm}^3$ ) was ignited from its short side by a 20 mm methane flame (flame application time: 3 s). The test was repeated 3 times for each formulation to ensure reproducibility; during the test, parameters, such as burning time, afterglow times, and final residue, were registered. Prior to flammability tests, samples were conditioned in climatic chamber at  $23^\circ\text{C}$  and 50% R. H.

### 2.5.12. TGA

Thermogravimetric analyses (TGA) have been carried out on a Q500 (by TA, Newcastle USA, weight sensitivity  $\pm 0.1 \mu\text{g}$ , dynamic baseline drift  $\pm 50 \mu\text{g}$  calculated by the producer using empty platinum pans in the range of temperature  $50\text{--}1000^\circ\text{C}$  with  $20^\circ\text{C}/\text{min}$ , no baseline correction and a temperature sensitivity of  $\pm 0.01^\circ\text{C}$ ). An aliquot of about 10 mg was placed in open alumina pans for each composition and heated from  $100$  to  $800^\circ\text{C}$  with a heating rate of  $10^\circ\text{C}/\text{min}$  in both  $\text{N}_2$  and air conditions ( $60 \text{ mL}/\text{min}$ ) after 30 min of isotherm treatment at  $100^\circ\text{C}$ . The final residue and TOCN percentage in the final residue have been calculated after taking into account the weight loss in the  $50\text{--}150^\circ\text{C}$  range because of water removal. Residue data at  $800^\circ\text{C}$  shown in Table S8 confirmed that the clay contents in the representative nanocomposites are in agreements with the theoretically clay loading ratio.

## 3. Results and discussion

TOCN/clay film preparation was carried out using three different clays of different aspect ratio. The MTM, SPN and mica nanoplatelets

have negative surface charge, and are exfoliated in colloidal dispersions by repeated shearing and sonication of the aqueous dispersion, which are the key factors to obtain well-dispersed clays. The TOCN also have negative charge so that electrostatic repulsion against exfoliated clay platelets in the colloid may improve dispersion of clay in the cellulose fibril matrix.

### 3.1. Colloidal properties of TOCN and 2D clay platelets

The TOCN/clay nanocomposites were prepared by a paper-related filtration process as described in the Experimental section and illustrated in Fig. 1a, to promote dispersion of exfoliated single platelets in the colloids. However, for mica, we did not succeed to make stable dispersions, although sedimentation in static condition was used to separate large aggregates. The zeta potential of TOCN, SPN, MTM and mica were  $-121$ ,  $-85.6$ ,  $-43.9$  and  $-38.2 \text{ mV}$ , respectively. The mixed TOCN/SPN and TOCN/MTM colloidal dispersions were transparent, whereas the turbidity of TOCN/mica was relatively high (Fig. 1b and c). Colloidal stability data are presented in Fig. S1. TOCN/SPN showed excellent stability, and TOCN/MTM also showed relatively good stability, whereas TOCN/mica showed moderate stability with some sedimentation after 10 days.

Atomic force micrographs of TOCN and clay suspension deposited on silicon wafer is shown in Figs. 1d and S2. The height of TOCN corresponds to  $2\text{--}3 \text{ nm}$  with a typical length range of  $500\text{--}700 \text{ nm}$  with some kinks (Zhou et al., 2020). The majority of SPN (width  $\sim 50\text{--}100 \text{ nm}$ ) and MTM platelets (width  $\sim 200\text{--}400 \text{ nm}$ ) appeared as  $\approx 1 \text{ nm}$  thick monolayers. Mica platelets had a width of  $1\text{--}2 \mu\text{m}$  with a thickness of

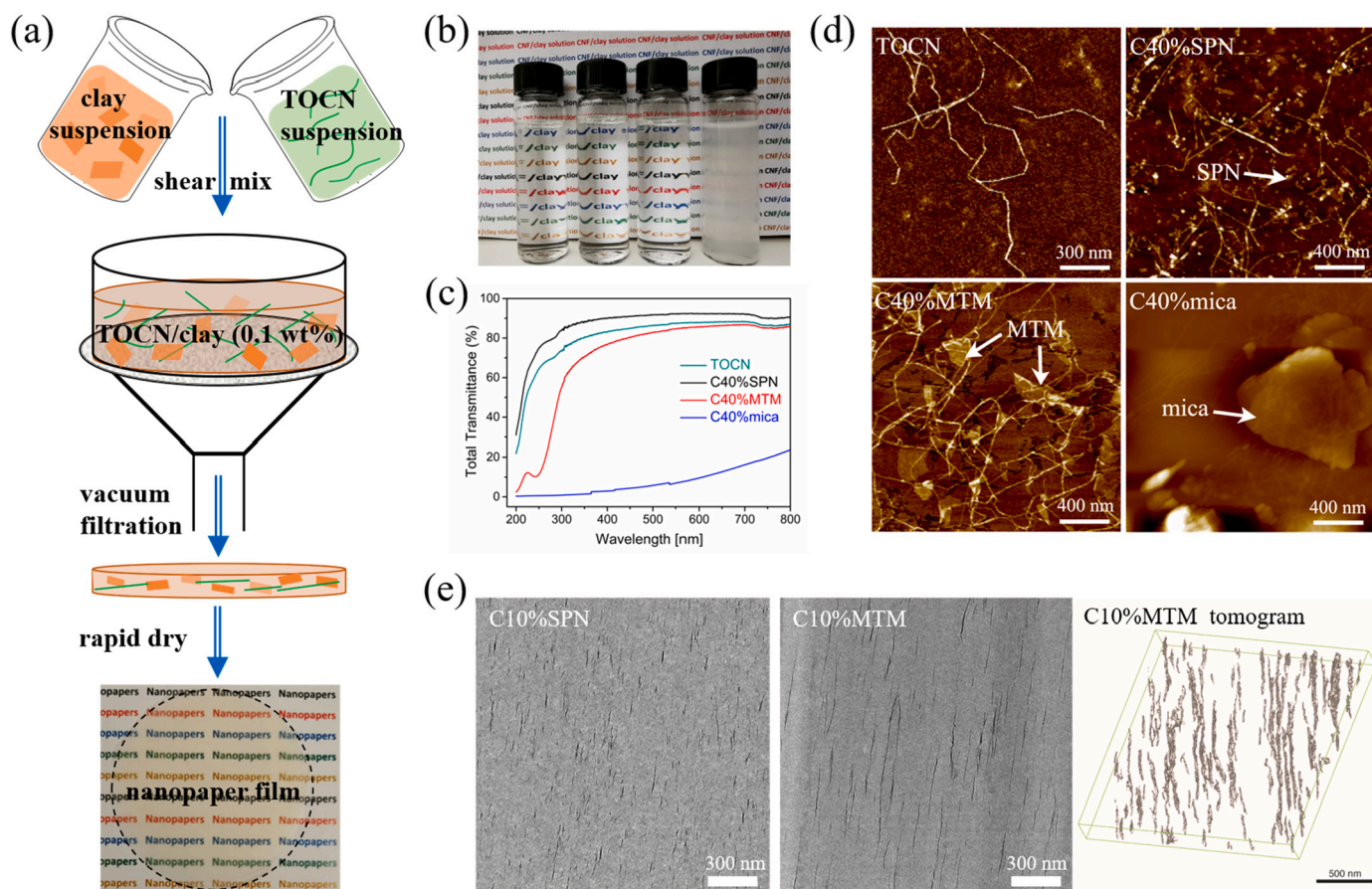


**Fig. 1.** (a) Preparation scheme of TOCN/clay nanocomposite films from TOCN/clay dispersion. (b) Neat hydrocolloids of TOCN, C40%SPN, C40%MTM and C40%mica (left to right) at 0.05 wt% concentration and (c) total optical transmittance spectra for fresh hydrocolloids (Fig. S1 shows photographs and spectra of these colloids after 10 days). (d) AFM images of neat TOCN, C40%SPN, C40%MTM and C40%mica samples. (e) TEM images of ultrathin sections of C10%SPN, C10%MTM in CNF matrix and the 3D tomogram of C10%MTM.

20–70 nm, and can be considered as multilayers. Herein, the aspect ratio of SPN, MTM and mica is about 75, 300 and 30, respectively.

### 3.2. Dispersion and orientation of clay platelets

The wet, filtered “cakes” were quickly dried within 15 min to form 30- $\mu\text{m}$  thick transparent films (Fig. 1a). Details of the nanocomposite structure were characterized since they controlled physical properties. Focus was on clay tactoids (stacks of agglomerated nanoplatelets), extent of horizontal orientation of clay platelets in the cross-sectional plane. The clay appears as dark streaks in the transmission electron

micrographs of ultra-thin cross-sections, due to the strong attenuation by the high-Z elements. A few-nanometers thick, well separated platelets are observed for SPN or MTM at volume fraction of 10% (C10%SPN and C10%MTM), see Fig. 1e. A 3D tomogram further verifies the well dispersed MTM. For mica (Fig. S3), even at 10 vol%, domains extending to a thickness up to half a micrometer are observed, with cracks induced during sectioning. The TOCN/MTM and TOCN/SPN nanocomposite films showed smaller scale resemblance to nacre’s “brick and mortar” organization, although the mortar content was very high. Orientated MTM was the “brick” and the TOCN phase served as the “mortar”.

A larger area was probed by X-ray diffraction with incident beam

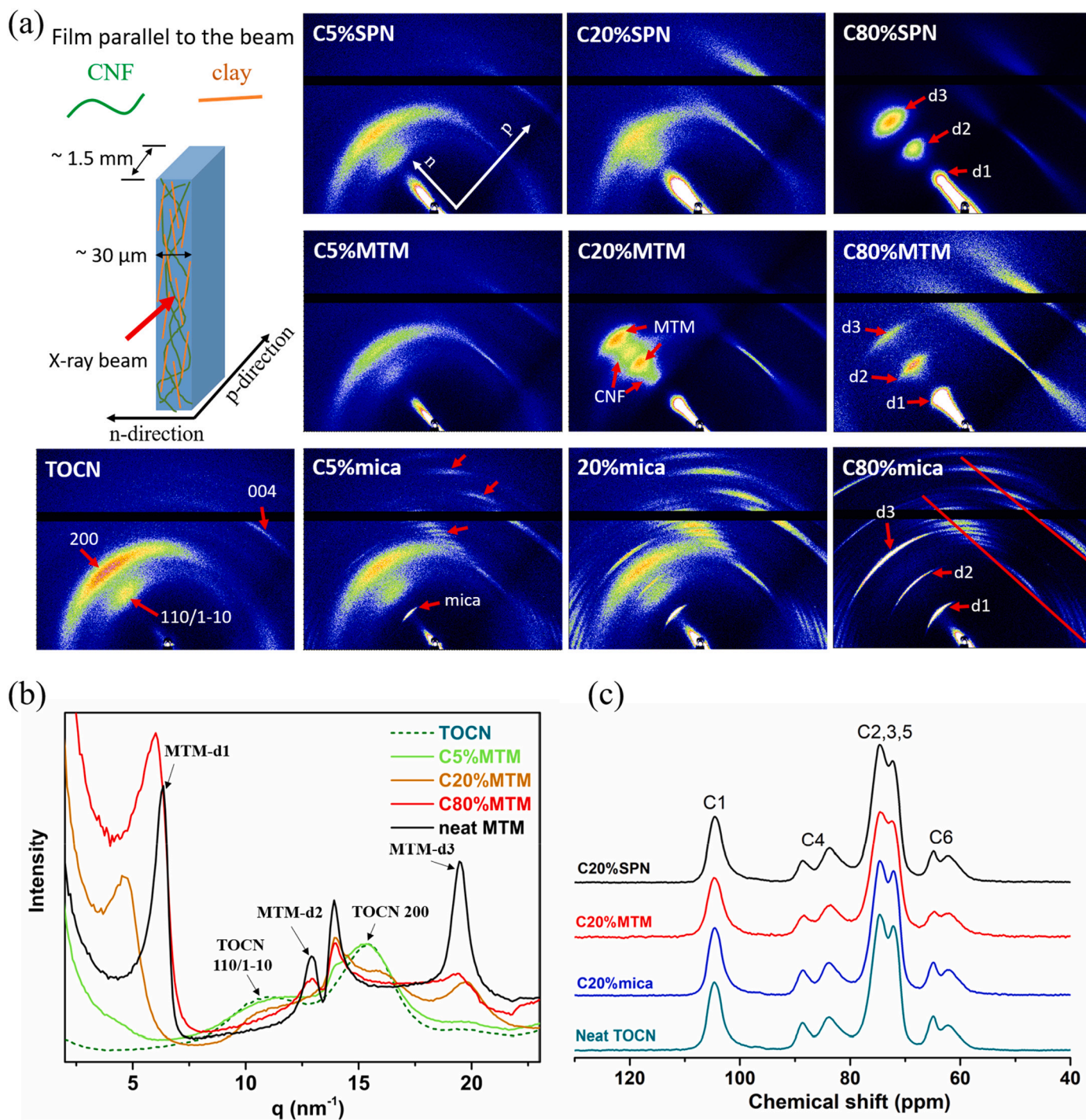


Fig. 2. Representative (a) 2D-WAXD patterns of TOCN/SPN, TOCN/MTM and TOCN/mica nanocomposite films. (b) Representative 1D-WAXD curves of TOCN/MTM. (c) Normalized Solid State NMR spectra of neat TOCN and TOCN/20 vol% clay composites.

parallel to the film. Fig. 2a shows representative 2D-WAXD patterns of TOCN/clays from low to high clay contents (for complete patterns, see Fig. S4). The film plane is oblique with respect to the detector, it is termed *p*-direction, and perpendicular to the film is termed *n*-direction.

Neat TOCN shows two diffraction arcs corresponding to 200 and 110/1–10 reflections, centered in *n*-direction and a 0 0 4 arc in the *p*-direction. The samples with 80% SPN, MTM or mica particles show three strong spots in *n*-direction, at roughly multiples of  $6.0 \text{ nm}^{-1}$  in the reciprocal space, indicating an interlayer distance of about 1 nm. We call the three spots *d*<sub>1</sub>, *d*<sub>2</sub>, *d*<sub>3</sub>. Along the *p*-direction, streaks can be seen for SPN and MTM at  $13.8^{-1}$  and  $24.1 \text{ nm}^{-1}$  from the center in the reciprocal space, indicating the two-dimensional order inside a single sheet without three-dimensional order. They correspond to the first two lattice point of a 2D hexagonal, whereas discrete crystalline spots are aligned on the layers (red lines) spaced at 13.8 nm and  $24.1 \text{ nm}^{-1}$  indicating the three-dimensional crystalline nature of mica.

At low SPN or MTM content (5 vol%), the diffraction patterns show minor changes compared to that of neat TOCN, although strong streak features are observed in the small angle scattering region perpendicular to the film. In contrast, C5% mica already shows sharp mica peaks (indicated by red arrows in Fig. 2a), at the same position as diffraction of C80% mica film. C20% MTM shows strong diffraction spots in *n*-direction, which are not present in TOCN films, indicating that some clay tactoids start to form. On the other hand, C20% SPN does not show the higher-order diffraction in *n*-direction, and thus single-SPN layers are still dispersed random in thickness direction.

The arc-like patterns along the azimuthal direction are characteristic of strong out-of-plane orientation of clay nanoplatelets at high concentration. The Herman's orientation factor with respect to the plane of the films surface was calculated (Fig. S5) and summarized in Table 1. The values of SPN and MTM were higher than 0.92, corresponding to misalignment values of about  $\pm 5\text{--}6^\circ$ , smaller than for the only previous report of similar data ( $\sim \pm 8\text{--}9^\circ$ ) (Medina, Nishiyama, et al., 2019).

The intensity profiles along *n*-direction of TOCN/MTM nanocomposites are summarized in Fig. 2b (complete data set in Fig. S6). C20% MTM shows peaks not present in the neat CNF films, which suggests that this is the clay volume fraction at which stacked MTM tactoids are beginning to form. With increased MTM content, more distinct MTM peaks were observed. Generally, sharper peaks correspond to larger crystallite size (Scherrer size) and more significant tactoid formation. Scherrer sizes of tactoids were estimated using peak widths of Gaussian functions fitted to characteristic peaks of SPN (*d*<sub>3</sub>), MTM (*d*<sub>3</sub>) and mica (*d*<sub>3</sub>). The estimated Scherrer sizes are listed in Table 1. Even high clay content C60% SPN and C80% SPN nanocomposites show a Scherrer size below 2 nm, corresponding to overlap of two layers of SPN. In the wider range of MTM contents (7.5–80 vol%), TOCN/MTM showed larger Scherrer size, with values from  $\sim 2$  to  $\sim 4$  nm, which still corresponds to tactoids of only  $\sim 4$  layers. In our previous enzymatic pretreated CNF (Enz CNF)/MTM ( $\text{Na}^+$ ) system (Medina, Nishiyama, et al., 2019), the

**Table 1**

Herman's orientation factor and Scherrer size of clay in the composites. Some values not included due to the absent or weak intensity of the *d*<sub>3</sub> peaks for fitting.

Clay content (vol%)	Herman's orientation factor			Scherrer size (unit: nm)		
	SPN- <i>d</i> <sub>3</sub>	MTM- <i>d</i> <sub>3</sub>	Mica- <i>d</i> <sub>3</sub>	SPN- <i>d</i> <sub>3</sub>	MTM- <i>d</i> <sub>3</sub>	Mica- <i>d</i> <sub>3</sub>
0	/	/	/	/	/	/
2.5	/	/	/	/	/	/
5	/	/	0.827	/	/	/
7.5	/	0.923	0.881	/	2.16	17.74
10	/	0.942	0.861	/	2.27	20.85
20	/	0.950	0.845	/	2.68	26.07
40	/	0.945	0.911	/	2.86	34.04
60	0.946	0.940	0.923	1.56	4.05	26.95
80	0.954	0.926	0.909	1.71	4.39	23.46

Scherrer size of the tactoids was 8–9 nm at MTM contents  $>50$  wt%, much larger than in the current TOCN-based nanocomposite. Enz CNF has larger lateral size than the current TEMPO oxidized CNF (Fig. S2); and the previous MTM aspect ratio was around 100, compared to current aspect ratio of  $\sim 200\text{--}400$ . The smaller lateral size of MTM favors tactoid formation due to increased mobility. Smaller lateral nanofiber dimension in the present study contributes to separation of MTM sheets. The present TOCN also has higher surface charge than Enz CNF, which improves colloidal stability and local nematic order for better packing.

### 3.3. Reduced cellulose crystallinity with clay content

Compared to neat TOCN, (200) peaks of cellulose in the composites (Fig. S6) are broader and gives smaller Scherrer size. This change in crystallite size is possibly caused by mechanical constraints of TOCN fibrils due to the presence of clay platelets. Solid-State NMR spectroscopy was carried out to clarify this. Fig. 2c shows NMR spectra of TOCN/20% clay nanocomposites. The crystal index of TOCNs (Table 2) was determined from the C4 region of NMR spectra by using Pseudo-Voigt function (as described in Fig. S7) (Earl & Vanderhart, 1982; Newman, 1999). The TOCN in C20% MTM has the lowest crystal index. This could also be due to plastic deformation of TOCN from capillary forces during drying (Ogawa et al., 2020). MTM has the highest aspect ratio of investigated clay nanocomposites, so that such an effect may be strongest in TOCN/MTM. The lower crystallinity index for well-dispersed 20% MTM (and SPN) compared with 10% compositions, shows the effect of clay content on space constraint for TOCN.

### 3.4. Stress-strain behavior and mechanical properties

For materials design purposes, nanocomposites from a wide range of clay contents were investigated. Stress-strain curves and mechanical property data are summarized in Figs. 3a–h, S8 and Tables S1–S3. TOCN films have random in-plane orientation of nanofibrils, and very low porosity. They show reasonably high modulus ( $\approx 14$  GPa) and strength ( $\approx 310$  MPa) at 50% RH, with plastic yielding followed by linear strain-hardening and ultimate fracture. Biaxially oriented polyethylene terephthalate (BOPET) films qualitatively show similar behavior, but with higher strain to failure (Hashemi & Xu, 2007). When clay content is low ( $\leq 20$  vol%), the TOCN/SPN (Fig. 3a) and TOCN/mica (Fig. S8) nanocomposites show distinct yielding and strain hardening, with similar, fairly high strain to failure (Fig. 3f). Well-dispersed TOCN/MTM (Fig. 3c) with high platelet aspect ratio exhibit lower strain to failure, perhaps related to platelet fracture. With higher clay content ( $>20$  vol%), TOCN/MTM (Fig. 3d) shows transition to brittle behavior, but also high strength, exceeding 300 MPa for C40% MTM (40 vol% clay). It is interesting that nanocomposites from SPN, with lower aspect ratio than MTM, strength is reduced, plastic yielding is distinct (“knee” in stress-strain curve) and increased ductility (strain to failure) (Fig. 3b), associated with platelet pull-out mechanisms. By selecting appropriate platelet aspect ratio, it is possible to optimize the strength-toughness (ductility) balance.

If platelet nanocomposites obey composite micromechanics (Christensen, 1979, 2005), a linear relationship is expected between clay volume fraction and Young's modulus. Since Fig. 3g shows non-linear relationships, effects from nanostructural agglomerates correlates with less effective platelet reinforcement. Tactoids have lower effective stiffness due to weak interplatelet adhesion, and imperfect geometrical

**Table 2**

Crystallinity index from SS-NMR spectra.

Clay content (vol%)	TOCN/SPN	TOCN/MTM	TOCN/mica
0	0.27	0.27	0.27
10	0.23	0.22	/
20	0.20	0.18	0.27

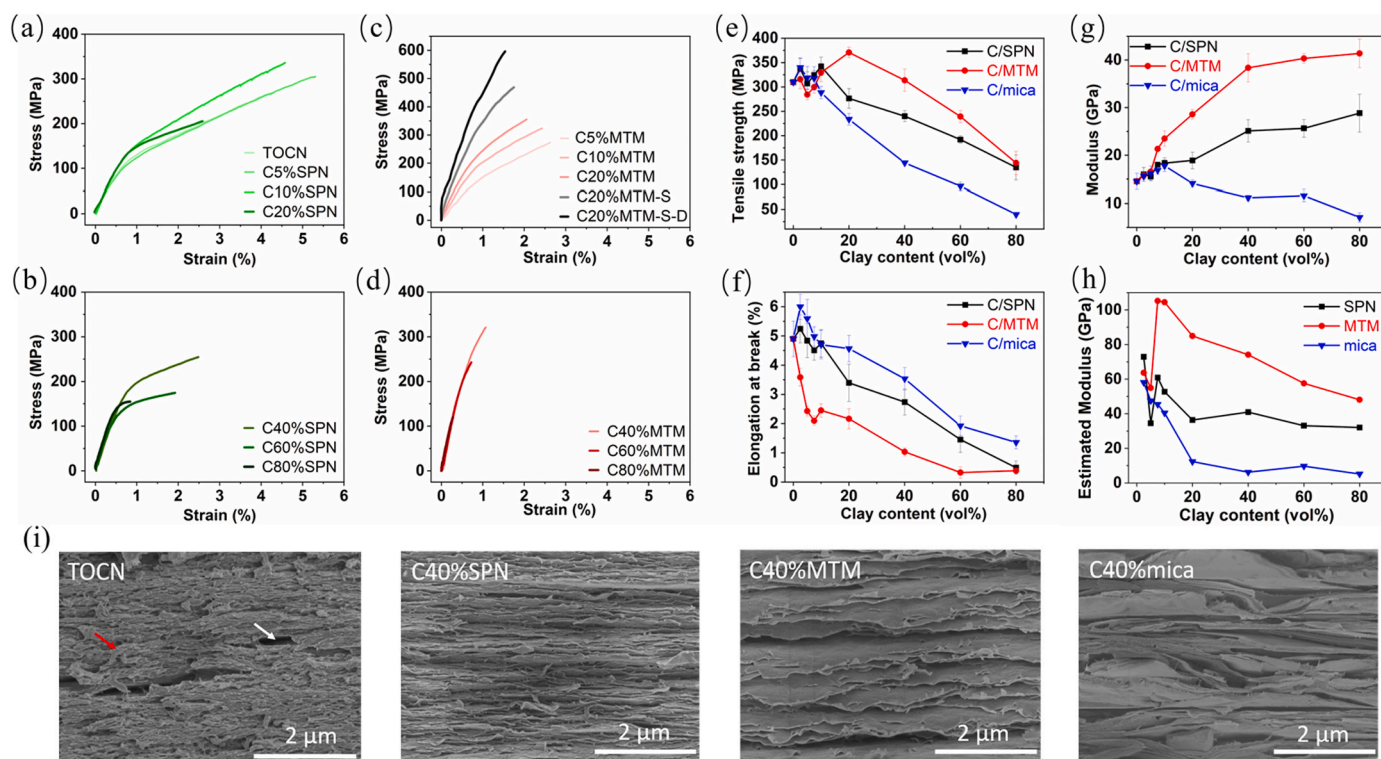


**Fig. 3.** Representative stress-strain curves of 0–80 vol% (a) TOCN/SPN, (b) TOCN/MTM (c) Tensile strength, (d) Elongation at break, (e) Young's modulus and (f) Estimated effective modulus of clays as a function of clay content. The tensile testing performed in 50%RH condition. C20%MTM-S is small specimen, C20%MTM-S-D means small specimen measured in dry condition. (g) Fracture surfaces of neat TOCN, C40%SPN, C40%MTM and C40%mica samples.

matching (each platelet in the stack has different geometry). This also leads to poor stress transfer and lowered reinforcement effect. The lowest reinforcement effect in Fig. 3g for TOCN/mica, with large mica tactoids, supports this interpretation. The absolute Young's modulus is particularly high for TOCN/MTM above 10 vol% clay content, with well-dispersed platelets of higher aspect ratio than for TOCN/SPN.

An interesting achievement is the continuous increase in modulus with MTM and SPN clay content all the way up to 80 vol% (Fig. 3g), in contrast to previous work (Das et al., 2013; Ho et al., 2012; Medina, Nishiyama, et al., 2019; Wang et al., 2013; Zerda & Lesser, 2001). The

rule of mixtures was used to determine effective clay modulus, see Supporting information. Effective moduli of SPN, MTM and mica at different volume fractions are provided in Fig. 3h. The values are high, but lower than theoretical predictions of clay modulus, which are 170–270 GPa (Chen & Evans, 2006; Manevitch & Rutledge, 2004; Sayers & den Boer, 2016). When the MTM content is 7.5 and 10 vol%, the effective  $E_{MTM}$  has the highest values of more than 100 GPa. No chemical linking is introduced between TOCN and clay, since this would reduce the recycling potential. Instead the high effective  $E_{MTM}$  is related to good dispersion of MTM monolayers, with intercalated TOCN fibrils and high

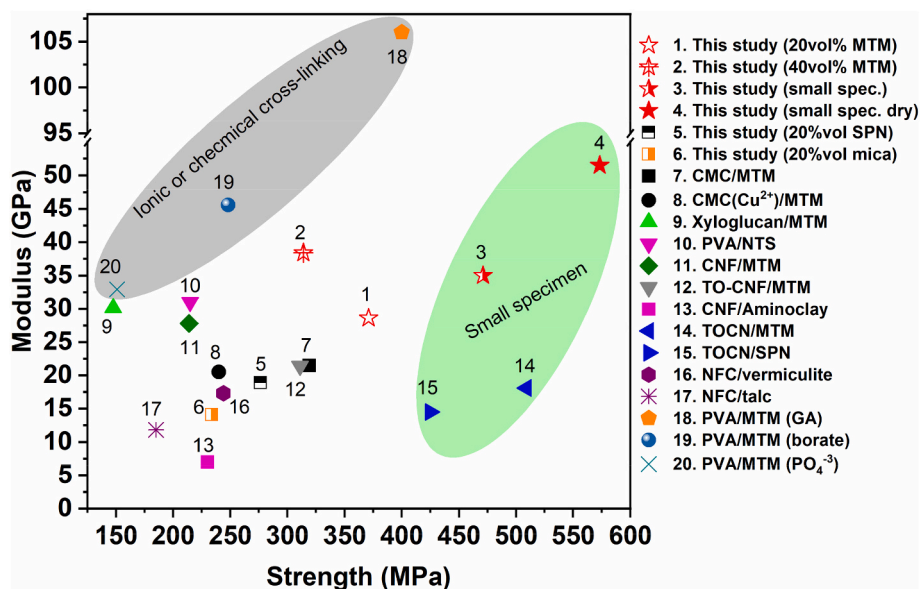


**Fig. 4.** Graphical comparison of the Young's modulus and ultimate strength of the present TOCN/MTM nanocomposites with other clay/polymer composites, CMC/MTM (Das et al., 2013), CMC(Cu<sup>2+</sup>)/MTM (Das & Walther, 2013), Xyloglucan/MTM (Kochumalayil et al., 2013), PVA/NTS (Das et al., 2015), CNF/MTM (Medina, Nishiyama, et al., 2019), TO-CNF/MTM (Xu et al., 2021), CNF/Aminoclay (Liu, Yu, & Bergström, 2018), TOCN/MTM (Wu et al., 2012), TOCN/SPN (Wu et al., 2014), NFC/vermiculite (Aulin et al., 2012), NFC/talc (Liimatainen et al., 2013), PVA/MTM (Podsiadlo et al., 2007), PVA/MTM (GA) (Podsiadlo et al., 2007), PVA/MTM (borate) (Walther, Bjurhager, Malho, Pere, et al., 2010), PVA/MTM (PO<sub>4</sub><sup>-3</sup>) (Walther, Bjurhager, Malho, Ruokolainen, et al., 2010). Detailed mechanical properties parameters are listed in Table S4. Abbreviations: PVA: poly(vinyl alcohol); NTS: sodium tetrasilicic mica; GA: glutaraldehyde.

in-plane clay platelet (and TOCN) orientation, as supported by WAXD and SEM results.

The present properties are remarkable, in that high ultimate strength (Fig. 3e),  $\approx 370$  MPa is combined with high Young's modulus  $\approx 25$  GPa at C20%MTM. For C40%MTM, the strength is  $\approx 310$  MPa at 38 GPa modulus. These data are much higher than previous polymer/clay and TOCN/clay data presented in Fig. 4 and listed in Table S4. The exceptions are very thin PVA/MTM LbL-assembled films enhanced by glutaraldehyde (Podsiadlo et al., 2007) and borate (Walther, Bjurhager, Malho, Pere, et al., 2010) cross-linking (materials 18 and 19 in Fig. 4). Probably, the “crosslinking” effect primarily improves stress transfer by introducing covalent bonds at the polymer/clay interface, and reduces effects from interfacial moisture. For the cellulosic TOCN matrix, the best ultimate strength reports are for thin TOCN/SPN (Wu et al., 2014) and TOCN/MTM (Wu et al., 2012) films with low clay content (10 wt% SPN and 5 wt% MTM) (materials 14 and 15 in Fig. 4), but these results may also be related to specimen size effects.

For the high-strength reports, specimen size was much smaller than here. For clarification of this effect, we prepared thin C20%MTM films of similar thickness (7–8  $\mu\text{m}$ ) and the same small specimen geometry as in previous studies (Wu et al., 2012; Wu et al., 2014). These films showed an ultimate strength of  $\approx 470$  MPa with a modulus of up to 35 GPa at 50% RH. Moisture effects have been discussed recently, with respect to ductility (Hou et al., 2021). In dry condition, the strength was increased

to 573 MPa with a modulus exceeding 50 GPa, see material 4 in Fig. 4, which is even higher than the best previous TOCN/clay reports. Strength apparently shows strong dependence on specimen geometry, as expected for brittle materials (Ashby & Jones, 2012), and reported tensile strengths are not intrinsic material properties. Strength is controlled by defects, and the probability of having large defects increases with specimen size. The key observation from Fig. 2 and Table 1, is that high clay content, high aspect ratio, good dispersion and high out-of-plane orientation of both clay and TOCN in the present nanocomposites translates into exceptionally high Young's modulus and tensile strength.

Fracture surface micrographs are presented in Fig. 3i. Neat TOCN shows almost micrometer sized TOCN bundle protrusions (red arrow) and holes (white arrow) corresponding to TOCN bundle pull-out. Fracture surfaces of SPN, MTM and mica nanocomposites are very different. In C40%SPN, surfaces show moderate roughness with nanolayered structures parallel to the film surface and short platelet pull-out lengths. For the more coarsely structured C40%mica, a substantial extent of mica tactoid pull-out takes place so that strain to failure is increased, see Fig. 3f. MTM fracture surfaces show characteristics between SPN and mica, yet dominated by the long pull-out lengths of straight, planar MTM platelets. The EDX images (Fig. S9) show that clays and TOCNs are uniformly distributed at microscale.

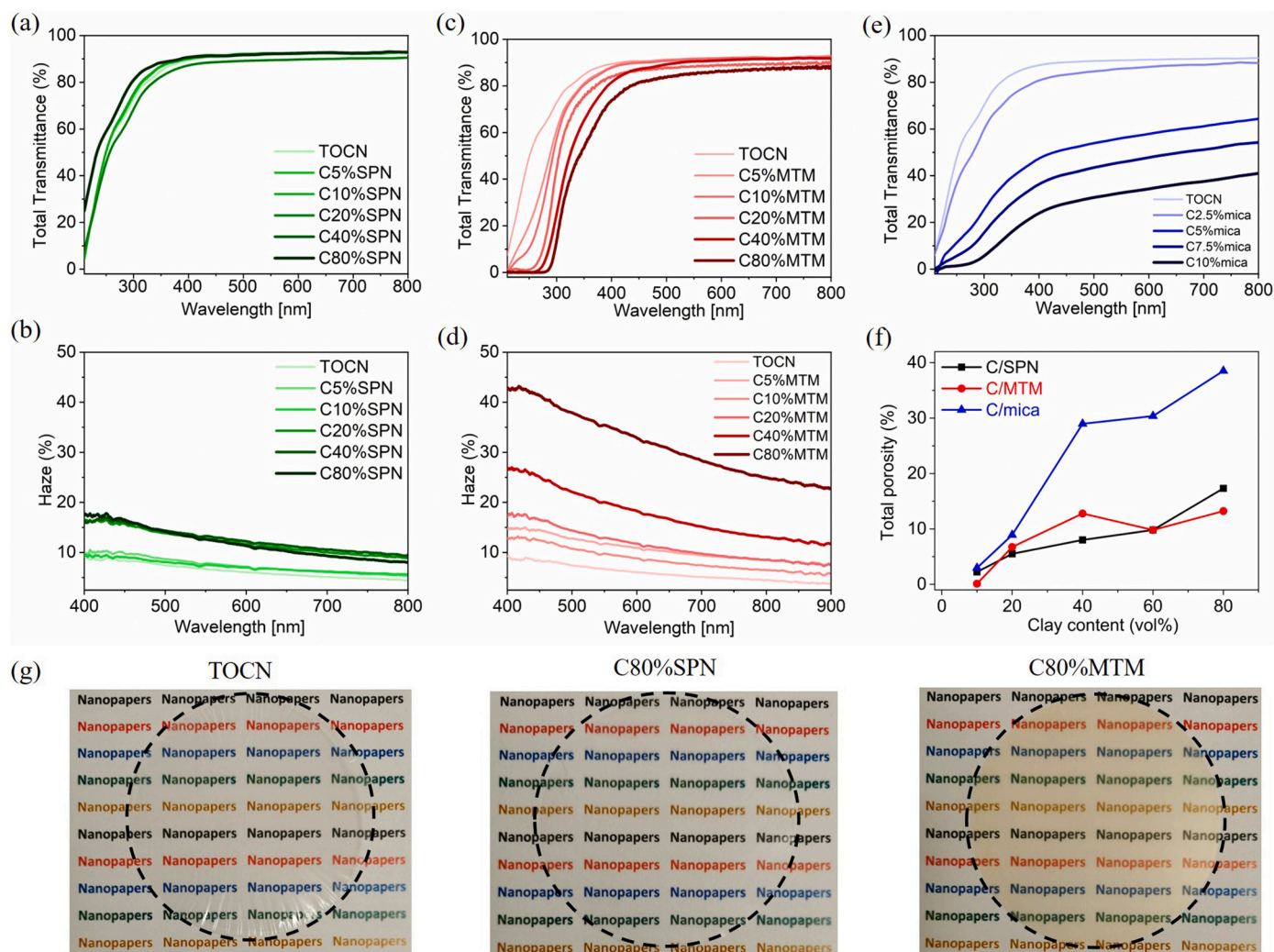


Fig. 5. UV-visible transmittances at  $\sim 30$   $\mu\text{m}$  thickness of (a) TOCN/SPN, (c) TOCN/MTM and (e) TOCN/mica. Haze as a function of wavelength of (b) TOCN/SPN and (d) TOCN/MTM. (f) Total porosity of TOCN/SPN, TOCN/MTM and TOCN/mica nanocomposite films with different clay contents. (g) Representative photographs of TOCN/clay films, neat TOCN, C80%SPN and C80%MTM show prominent transparency.

### 3.5. Optical and UV shielding properties - nanostructural effects

High optical transmittance is important for use of TOCN/clay in optoelectronic devices, and for some gas barrier coatings; it should also be sensitive to clay dispersion. UV-shielding is critical for liquid packaging (orange juice) films replacing aluminium barriers. Optical and ultraviolet shielding properties are presented in Fig. 5. The addition of SPN and MTM is not influencing optical transmittance of nanopaper films very much in the visible range (Fig. 5a and c). Even with clay content up to 80 vol% (corresponding to 88 wt%), the composite films still show high transmittance, and somewhat higher for SPN. In previous studies (Das et al., 2015; Medina, Nishiyama, et al., 2019; Wu et al., 2012; Wu et al., 2014), high clay content resulted in significantly decreased transmittance in visible range. The improvement of transmittance is attributed to the thinner tactoids (Table 1) in the present nanocomposites, as determined by WAXD. The UV transmittance of TOCN/MTM films was greatly reduced for nanocomposites containing 20–80 vol% MTM, so that optical transmittance is combined with UV-light protection, a comparison of the UV-shielding properties between

present study and literatures are listed in Table S5. For TOCN/mica films (Fig. 5e), even low mica content reduced the transmittance, a consequence of light scattering due to thicker tactoids. Haze measurements show the fraction of transmitted light scattered at larger scattering angles, an indirect measure of nanostructural homogeneity in the films. The haze of TOCN/SPN films (Fig. 5b) is at similar values for 0–10 vol% clay, but in the 20–80 vol% range, the haze increases almost step-wise, perhaps by scattering from tactoids. The haze for TOCN/MTM (Fig. 5d) increases monotonously with MTM content, and this is related to scattering from larger clay platelets, and possibly tactoids and some voids at higher clay content.

### 3.6. Porosity effects

In Fig. 5f, the total porosity is reported based on weight and dimensions of the samples. At higher clay content, pores will form for geometric reasons related to packing of 1 nm thick platelets, since the fraction of  $\approx 3$  nm diameter TOCN fibrils able to fill empty space is decreased. The TOCN/mica composites show high porosity, which also

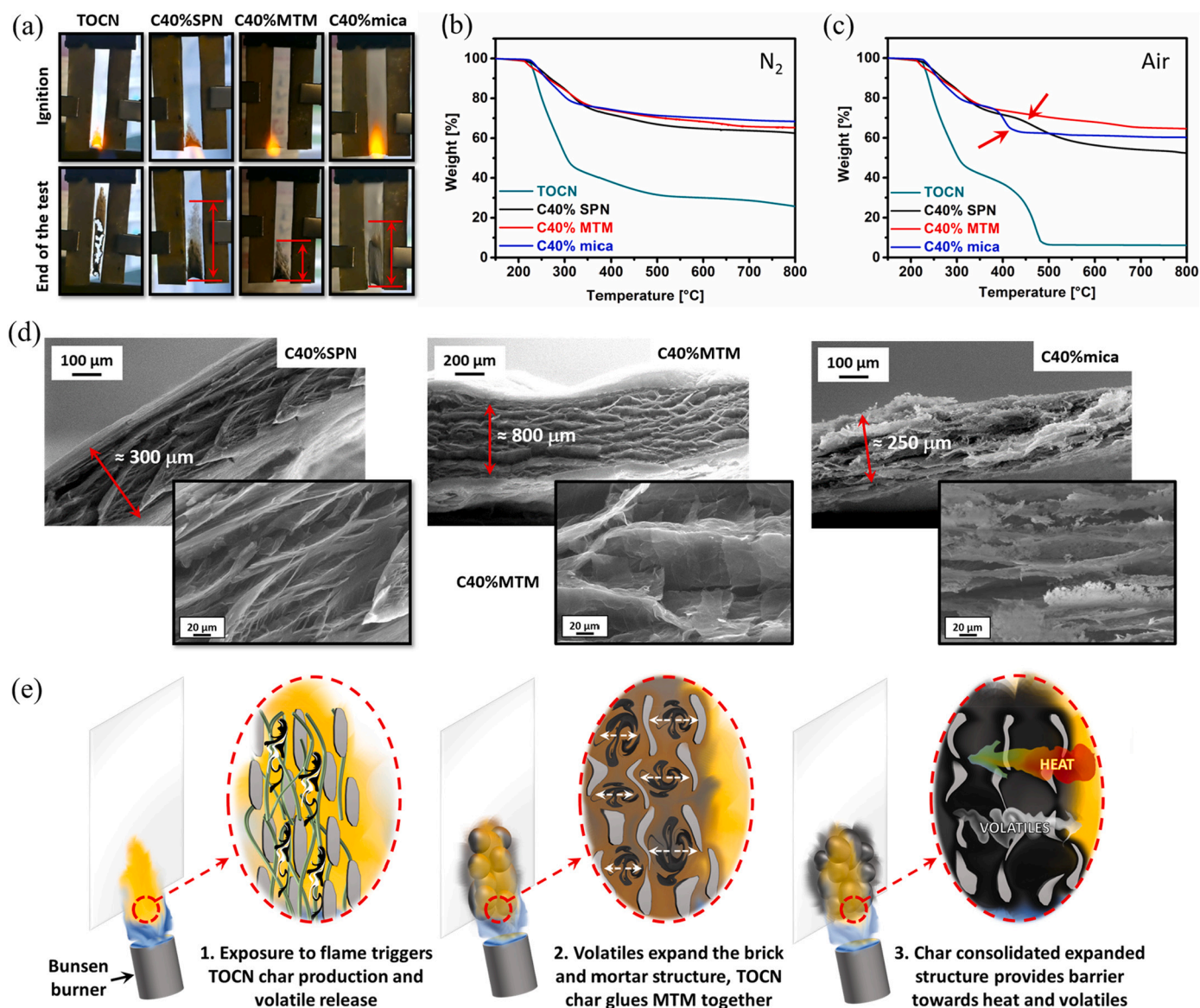


Fig. 6. Fire retardancy characterization: (a) snapshot of flammability test in vertical configuration of neat TOCN, C40%SPN, C40%MTM, and C40%mica samples. (b) TGA in nitrogen atmosphere, (c) TGA in air, (d) Post combustion cross-section SEM micrographs of composites at 40% clay. (e) Scheme illustration of TOCN/MTM expansion process.

decreases mechanical properties at high mica content. In contrast, porosity values for SPN and MTM nanocomposites are below 20%, although porosity increases with clay content. Decrease in strength and strain to failure are partly due to increased porosity, and porosity also contributes to haze (Medina, Nishiyama, et al., 2019). At high clay content, the distribution of the CNF matrix will also be less favorable, with compromised stress transfer from the TOCN matrix to clay platelets.

### 3.7. Fire retardancy (FR) and thermal properties

The toxicity of halogen and phosphorous fire retardants motivates investigations of eco-friendly alternatives. Horizontal and vertical flammability tests were performed to determine the propensity of TOCN/clay composites to initiate fire when exposed to a small flame (Table S6). Neat TOCN is easily ignited with flames spreading on the sample before self-extinguishing and an afterglow phenomenon (oxidation in the absence of flame) further consuming the sample (Fig. S10). This phenomenon is seen in horizontal tests (Fig. S10), but not in vertical configuration (Fig. 6a). Clay platelets strongly improve fire retardancy. Stratified clay platelets hinder oxygen diffusion, reduces oxidation rate and delays evaporation of volatiles. Interestingly, fire retardant properties not only depend on clay content and aspect ratio but also on dispersion. TOCN/MTM can self-extinguish the flame or even show “no ignition”, thus ensuring the highest level of fire safety. SPN and mica composites achieve performance similar to MTM only in horizontal configuration. In vertical flame test, although the flame is self-extinguished upon flame removal, part of the SPN and mica samples still catch fire, as demonstrated by the different lengths burned (Fig. 6a).

All clay nanocomposites showed favorable intumescent behavior. During flame exposure, the volatiles released from TOCN decomposition remain trapped by clay platelets, causing nanocomposite expansion in thickness direction (Alongi et al., 2015). This limits the amount of volatiles feeding the flame and leads to self-extinguishing. The expansion is clearly visible for MTM-containing composites but is less apparent for SPN and mica. Residues collected from vertical flame tests were investigated by SEM (Fig. 6d). A clear increase in thickness and formation of an expanded cellular structure was observed for all samples. The average thickness was estimated to be 300, 800 and 250  $\mu\text{m}$  for SPN, MTM and mica, respectively. SPN and MTM composites produced a more regular and homogeneous expansion with the highest porosity in TOCN/MTM. Conversely, mica residues displayed an irregular and damaged structure with a broad distribution of pore sizes. The high aspect ratio and excellent dispersion of MTM platelets contributes to the strong fire-retardant behavior in TOCN/MTM, without any use of toxic flame retardant additives.

Mechanisms of fire retardancy (FR), were investigated by thermogravimetric analysis (TGA). Clay differences do not change the decomposition behavior of TOCN in inert atmosphere; it occurs in one step (Fig. 6b). In oxidative environment (Fig. 6c), well-dispersed, high aspect ratio MTM can suppress the second weight loss step by forming a barrier to oxygen diffusion (Carosio et al., 2015). In contrast, in SPN and mica nanocomposites the oxidation barrier is less efficient and an oxidation step is apparent (see arrows in Fig. 6c). For SPN, the reason is the lower aspect ratio and for mica it is the poor dispersion (Wu et al., 2012; Wu et al., 2014). Complete analysis of TGA data (Figs. S11 and S12, Tables S7 and S8) and discussion of mechanisms are presented in Supporting information. A correlation is thus established between the composite structure and the superior FR properties of MTM-containing samples. The excellent nanoscale dispersion and preferential orientation of MTM provide a high density of TOCN/MTM interfaces homogeneously distributed throughout the thickness of the composite. This maximizes the expansion of the structure (+2600%) during flame exposure. As demonstrated in Fig. 6e, the MTM high aspect ratio favors the buildup of pore walls where the char produced by TOCN holds the MTM platelets together. The resulting structure reduces heat transfer

and prevents evaporation of volatiles, while showing a surprising resistance to oxidation. This completely prevents flame spreading and results in safer FR performance in the nanocomposites.

### 3.8. Recycling

The present TOCN/clay nanocomposites are recyclable. Previously, we attempted to recycle MTM composites with enzyme pretreated CNF. It is difficult to redispersed cellulose and MTM in water, probably due to “cocrySTALLIZATION” and agglomeration of individual fibrils. In contrast, the present TOCN/clay nanocomposites can be readily redispersed in water through simple soaking and shear mixing. Highly charged, neat TOCN films are also redispersible and recyclable (Yang et al., 2020). Here, the same characteristics was found in nanocomposites with well-dispersed clay nanoplatelets (Fig. 7a), since the interface between TOCN and clay is of physical nature. We selected C20%MTM (Fig. 7b and c, Table S9) and subjected this composition to several rounds of recycling. The optical transmittance maintains similar values after two rounds of recycling. Also, after two rounds of recycling, Young's modulus and ultimate strength are not dramatically reduced. After three rounds of recycling, mechanical properties decreased significantly, and optical transmittance was also reduced. This was due to increased porosity (Table S9). Possibly, impaired dispersion influences capillary force effects and packing during drying, so that porosity is increased.

We note that the present nanocomposites have favorable eco-friendly characteristics and are recyclable. Since properties are sensitive to moisture, this is a limitation for some applications. Gas barrier properties are reduced at higher relative humidity, although less so than for neat CNF films (Liu et al., 2011). We have reported the modulus of cellulose nanofibrils reinforced by 20 vol% MTM to be 35 GPa at 50% RH but 50 GPa under dry conditions. This lowering of modulus is related to moisture located at the interface of polysaccharides/MTM (Wang, Wohler, et al., 2014), which reduces interfacial stress transfer. Covalent links at the interface (Podsiadlo et al., 2007; Yao et al., 2017) or addition of epoxy (Medina, Ansari, et al., 2019) would address the problem, but also compromise recycling.

## 4. Conclusions

Extensive shearing, centrifugation and sonication of clay and cellulose nanofibril colloids were keys to achieve high-performance nanocomposites with well-dispersed and oriented clay platelet reinforcement up to 80 vol% content. The excellent clay nanoplatelet dispersion was verified by WAXD and TEM. The charge repulsion between cellulose and 2D clay nanoplatelets is a contributing factor. The process is scalable, and 100  $\mu\text{m}$  films are possible to process and stack to form thicker laminates.

Modulus values as high as 35–50 GPa and strengths 300–570 MPa were obtained for TOCN/MTM, because of clay platelet individualization, high in-plane orientation, high aspect ratio and high clay content. In addition, optical and fire-retardant properties were greatly improved by better clay dispersion, extending the property range. Such high absolute properties are rarely reported for macroscopic polymer nanocomposite films, in particular the modulus values at high MTM content are remarkable. The high in-plane modulus of the cellulose nanofibril “matrix” is helpful.

The high-aspect ratio cellulose/MTM films have significantly higher modulus than cellulose/SPN nanocomposites; this is a fact. Classical micromechanics theories are based on an assumption of perfect interface bonding, and do not predict any modulus effects for those materials with large aspect ratios. Most likely, the explanation is that interfacial matrix/platelet adhesion is not “perfect” in the present nanocomposites, as assumed in composite micromechanics theory. One reason is geometric, since random-in-plane cellulose fibrils with a diameter of 3–4 nm cannot perfectly cover 1 nm thick clay platelets at high clay content.

These transparent nanocomposites have potential exemplified by

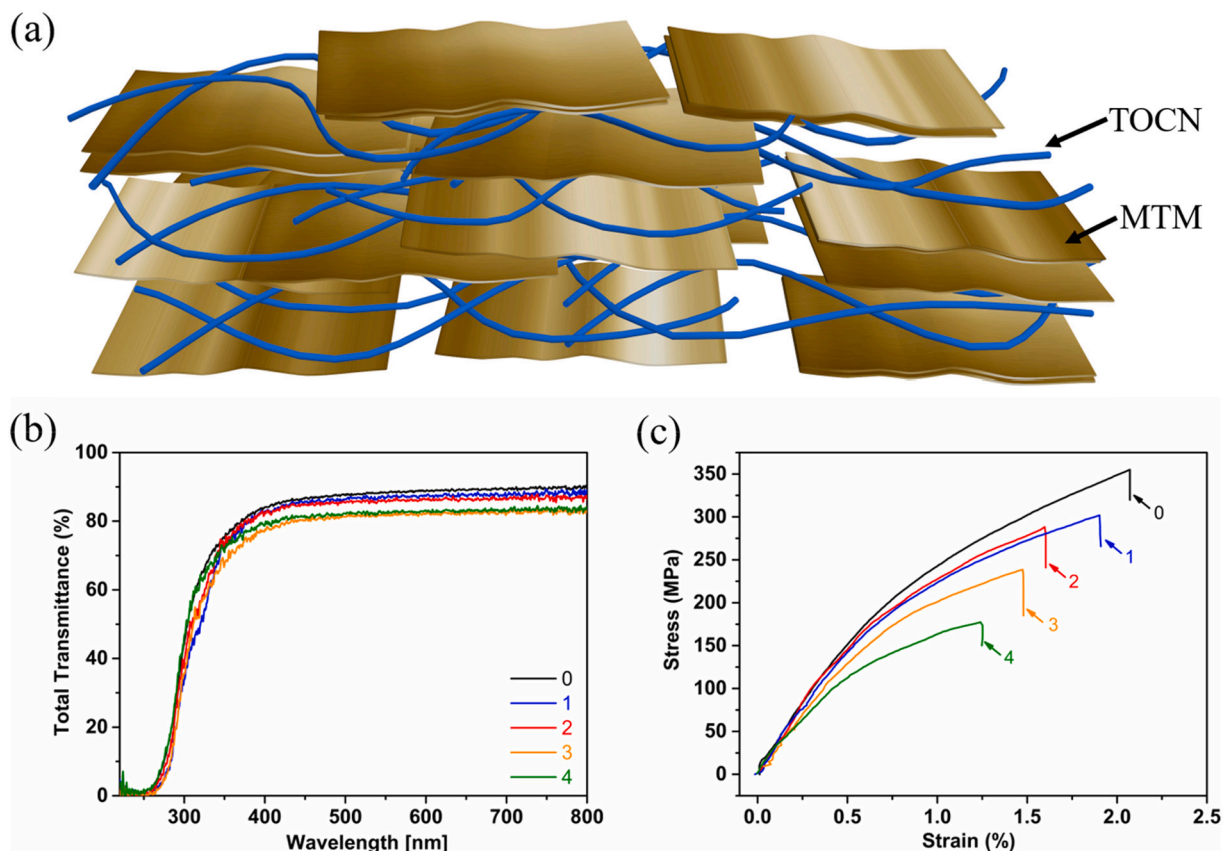


Fig. 7. (a) Illustration of TOCN and MTM organization in the nanocomposite. (b) Representative stress-strain curves and (c) optical transmittance of C20%MTM as a function of the number of recycling rounds.

films or coatings, eg replacing aluminium in liquid packaging, as fire retardant coatings of engineering or building materials and in photonic devices. For virtually all properties, the present results show strong effects from 2D platelet dispersion and/or out-of-plane orientation, identifying critical nanostructural parameters.

#### CRediT authorship contribution statement

**Lengwan Li:** Investigation, Conceptualization, Data curation, Formal analysis, Writing – original draft. **Lorenza Maddalena:** Data curation, Investigation. **Yoshiharu Nishiyama:** Data curation, Formal analysis, Writing – review & editing. **Federico Carosio:** Writing – review & editing, Resources. **Yu Ogawa:** Data curation, Investigation, Writing – review & editing. **Lars A. Berglund:** Conceptualization, Writing – review & editing, Supervision, Funding acquisition, Resources.

#### Acknowledgments

We acknowledge funding from KTH and Knut and Alice Wallenberg foundation through the Wallenberg Wood Science Center and the KAW Biocomposites program. Treesearch Research Infrastructure is acknowledged for their financial support of the WAXD analysis at Research Institutes of Sweden (RISE). The authors would also like to thank Assoc. Prof. Anita Telemann from RISE for the help in conducting the WAXD measurements. Lengwan Li acknowledges Asst. Prof. Yuan-yuan Li and Dr. Ramiro Rojas for assistance of CNF preparation. Hui Chen is acknowledged for optical transmittance measurements set up. Politecnico di Torino acknowledges the financial support from Italian Ministry of University (MUR) call PRIN 2017 with the project 2017LEPH3M “PANACEA. Ing. D. Pezzini and G. Iacono are acknowledged for SEM morphologies on vertical flame test residues and TGA

experiments respectively. The NanoBio-ICMG platform (FR 2607) is acknowledged for granting access to the electron microscopy facility.

#### Appendix A. Supplementary data

Method to estimate the effective Young's modulus of clay. Photographs and spectra of TOCN/clay solutions (Fig. S1). AFM height images (Fig. S2). TEM image of C10%mica (Fig. S3). 2D-WAXD patterns of TOCN/clay films (Fig. S4). Example of WAXD reduction method and I-A curves (Fig. S5). 1D-WAXD curves of TOCN/clay films (Fig. S6). Example of the method to calculate crystal index from NMR curves (Fig. S7). Stress-strain curves of TOCN/mica films (Fig. S8). SEM images of the fracture surface and EDX mapping (Fig. S9). Snapshot from TOCN flammability test in horizontal configuration (Fig. S10). Thermogravimetric data of CNF/clay in  $N_2$  (Fig. S11), in Air (Fig. S12) and analysis. Mechanical properties parameters of TOCN/clay films (Tables S1–S3). Mechanical properties of present study and literature data (Table S4). UV-shielding properties of present study and literature data (Table S5) Horizontal and Vertical flammability test results (Table S6). Thermogravimetric data (Tables S7–S8). Mechanical properties parameters of C20%MTM after recycling (Table S9). Supplementary data to this article can be found online at <https://doi.org/10.1016/j.carbpol.2021.119004>.

#### References

- Alongi, J., Han, Z., & Bourbigot, S. (2015). Intumescence: Tradition versus novelty. A comprehensive review. *Progress in Polymer Science*, 51, 28–73.
- Ashby, M. F., & Jones, D. R. H. (2012). Chapter 15 - Probabilistic fracture of brittle materials. In M. F. Ashby, & D. R. H. Jones (Eds.) (4th ed., 1. *Engineering materials* (pp. 219–228). Boston: Butterworth-Heinemann.
- Aulin, C., Salazar-Alvarez, G., & Lindstrom, T. (2012). High strength, flexible and transparent nanofibrillated cellulose-nanoclay biohybrid films with tunable oxygen and water vapor permeability. *Nanoscale*, 4(20), 6622–6628.

- Benítez, A. J., & Walther, A. (2017). Cellulose nanofibril nanopapers and bioinspired nanocomposites: A review to understand the mechanical property space. *Journal of Materials Chemistry A*, 5(31), 16003–16024.
- Berglund and Liu, 2014. Berglund A Liu. Strong nanopaper. U.S. Patent: US20120216718A1, Feb 25, 2014.
- Carosio, F., Kochumalayil, J., Cuttica, F., Camino, G., & Berglund, L. (2015). Oriented clay nanopaper from biobased components—Mechanisms for superior fire protection properties. *ACS Applied Materials & Interfaces*, 7(10), 5847–5856.
- Carosio, F., Kochumalayil, J., Fina, A., & Berglund, L. A. (2016). Extreme thermal shielding effects in nanopaper based on multilayers of aligned clay nanoplatelets in cellulose nanofiber matrix. *Advanced Materials Interfaces*, 3(19), 1600551.
- Carosio, F., Laufer, G., Alongi, J., Camino, G., & Grunlan, J. C. (2011). Layer-by-layer assembly of silica-based flame retardant thin film on PET fabric. *Polymer Degradation and Stability*, 96(5), 745–750.
- Chen, B., & Evans, J. R. G. (2006). Elastic moduli of clay platelets. *Scripta Materialia*, 54(9), 1581–1585.
- Christensen, R. M. (1979). *Mechanics of composite materials*. New York, NY: Wiley-Interscience.
- Christensen, R. M. (2005). *Mechanics of composite materials. Chapter 4.5*.
- Das, P., Malho, J. M., Rahimi, K., Schacher, F. H., Wang, B., Demco, D. E., & Walther, A. (2015). Nacre-mimetics with synthetic nanoclays up to ultrahigh aspect ratios. *Nature Communications*, 6, 5967.
- Das, P., Schipmann, S., Malho, J. M., Zhu, B., Klemradt, U., & Walther, A. (2013). Facile access to large-scale, self-assembled, nacre-inspired, high-performance materials with tunable nanoscale periodicities. *ACS Applied Materials & Interfaces*, 5(9), 3738–3747.
- Das, P., & Walther, A. (2013). Ionic supramolecular bonds preserve mechanical properties and enable synergetic performance at high humidity in water-borne, self-assembled nacre-mimetics. *Nanoscale*, 5(19), 9348–9356.
- Dzenis, Y. (2008). Structural nanocomposites. *Science*, 319(5862), 419–420.
- Earl, W. L., & Vanderhart, D. L. (1982). Measurement of <sup>13</sup>C chemical shifts in solids. *J. Magn. Reson.* (1969), 48(1), 35–54.
- George, J., & Ishida, H. (2018). A review on the very high nanofiller-content nanocomposites: Their preparation methods and properties with high aspect ratio fillers. *Progress in Polymer Science*, 86, 1–39.
- Hashemi, S., & Xu, Y. (2007). Thermal effects on fracture of biaxial-oriented poly (ethylene terephthalate) (BOPET) film. *Journal of Materials Science*, 42(15), 6197–6204.
- Ho, T. T. T., Zimmermann, T., Ohr, S., & Caseri, W. R. (2012). Composites of cationic nanofibrillated cellulose and layered silicates: Water vapor barrier and mechanical properties. *ACS Applied Materials & Interfaces*, 4(9), 4832–4840.
- Hou, Y., Guan, Q.-F., Xia, J., Ling, Z.-C., He, Z., Han, Z.-M., & Wu, H. (2021). Strengthening and toughening hierarchical nanocellulose via humidity-mediated Interface. *ACS Nano*, 15(1), 1310–1320.
- Husband et al., 2015 JC Husband, SP, DR Skuse T Mtsi M Likitalo A Coles. Paper filler composition. U.S. Patent: US9127405B2, Sep 08, 2015.
- Kim, Y. S., Davis, R., Cain, A. A., & Grunlan, J. C. (2011). Development of layer-by-layer assembled carbon nanofiber-filled coatings to reduce polyurethane foam flammability. *Polymer*, 52(13), 2847–2855.
- Kochumalayil, J. J., Morimune, S., Nishino, T., Ikkala, O., Walther, A., & Berglund, L. A. (2013). Nacre-mimetic clay/xyloglucan bionanocomposites: A chemical modification route for hygromechanical performance at high humidity. *Biomacromolecules*, 14(11), 3842–3849.
- Kojima, Y., Usuki, A., Kawasumi, M., Okada, A., Fukushima, Y., Kurauchi, T., & Kamigaito, O. (1993). Mechanical properties of nylon 6-clay hybrid. *Journal of Materials Research*, 8(5), 1185–1189.
- Kumar, A., & Dixit, C. K. (2017). 3 - methods for characterization of nanoparticles. In S. Nimesh, R. Chandra, & N. Gupta (Eds.), *Advances in nanomedicine for the delivery of therapeutic nucleic acids* (pp. 43–58). Woodhead Publishing.
- Laufer, G., Kirkland, C., Cain, A. A., & Grunlan, J. C. (2012). Clay-chitosan nanobrick walls: Completely renewable gas barrier and flame-retardant nanocoatings. *ACS Applied Materials & Interfaces*, 4(3), 1643–1649.
- Li, K., Clarkson, C. M., Wang, L., Liu, Y., Lamm, M., Pang, Z., & Ozcan, S. (2021). Alignment of cellulose nanofibers: Harnessing nanoscale properties to macroscale benefits. *ACS Nano*, 15(3), 3646–3673.
- Li, Y.-C., Schulz, J., Mannen, S., Delhom, C., Condon, B., Chang, S., & Grunlan, J. C. (2010). Flame retardant behavior of polyelectrolyte–Clay thin film assemblies on cotton fabric. *ACS Nano*, 4(6), 3325–3337.
- Liimatainen, H., Ezekiel, N., Sliz, R., Ohenoja, K., Sirvio, J. A., Berglund, L., & Niinimäki, J. (2013). High-strength nanocellulose-talc hybrid barrier films. *ACS Applied Materials & Interfaces*, 5(24), 13412–13418.
- Liu, A., Walther, A., Ikkala, O., Belova, L., & Berglund, L. A. (2011). Clay nanopaper with tough cellulose nanofiber matrix for fire retardancy and gas barrier functions. *Biomacromolecules*, 12(3), 633–641.
- Liu, K., & Jiang, L. (2011). Bio-inspired design of multiscale structures for function integration. *Nano Today*, 6(2), 155–175.
- Liu, P., Cottrill, A. L., Kozawa, D., Koman, V. B., Parviz, D., Liu, A. T., & Strano, M. S. (2018). Emerging trends in 2D nanotechnology that are redefining our understanding of “nanocomposites”. *Nano Today*, 21, 18–40.
- Liu, Y., Yu, S.-H., & Bergström, L. (2018). Transparent and flexible nacre-like hybrid films of aminoacids and carboxylated cellulose nanofibrils. *Advanced Functional Materials*, 28(27), 1703277.
- Y.R.I. Ltd., Y. R. I. (2018). CNF (cellulose nanofiber) market in Japan: Key research findings 2018. [https://www.yanoresearch.com/en/press-release/show/press\\_id/1938](https://www.yanoresearch.com/en/press-release/show/press_id/1938).
- Manevitch, O. L., & Rutledge, G. C. (2004). Elastic properties of a single lamella of montmorillonite by molecular dynamics simulation. *The Journal of Physical Chemistry B*, 108(4), 1428–1435.
- Mastrorade, D. N. (2003). SerialEM: A program for automated tilt series acquisition on tecna microscopes using prediction of specimen position. *Microscopy and Microanalysis*, 9(S02), 1182–1183.
- Medina, L., Ansari, F., Carosio, F., Salajkova, M., & Berglund, L. A. (2019). Nanocomposites from clay, cellulose nanofibrils, and epoxy with improved moisture stability for coatings and semistructural applications. *ACS Applied Nano Materials*, 2(5), 3117–3126.
- Medina, L., Nishiyama, Y., Daicho, K., Saito, T., Yan, M., & Berglund, L. A. (2019). Nanostructure and properties of nacre-inspired clay/cellulose nanocomposites—Synchrotron X-ray scattering analysis. *Macromolecules*, 52(8), 3131–3140.
- Mianehrow, H., Lo Re, G., Carosio, F., Fina, A., Larsson, P. T., Chen, P., & Berglund, L. A. (2020). Strong reinforcement effects in 2D cellulose nanofibril–graphene oxide (CNF–GO) nanocomposites due to GO-induced CNF ordering. *Journal of Materials Chemistry A*, 8(34), 17608–17620.
- Nepal, D., Kennedy, W. J., Pachter, R., & Vaia, R. A. (2021). Toward architected nanocomposites: MXenes and beyond. *ACS Nano*, 15(1), 21–28.
- Newman, R. H. (1999). Estimation of the lateral dimensions of cellulose crystallites using <sup>13</sup>C NMR signal strengths. *Solid State Nuclear Magnetic Resonance*, 15(1), 21–29.
- Ogawa, Y., Nishiyama, Y., & Mazeau, K. (2020). Drying-induced bending deformation of cellulose nanocrystals studied by molecular dynamics simulations. *Cellulose*, 27(17), 9779–9786.
- Podsiadlo, P., Kaushik, A. K., Arruda, E. M., Waas, A. M., Shim, B. S., Xu, J., & Kotov, N. A. (2007). Ultrastrong and stiff layered polymer nanocomposites. *Science*, 318(5847), 80–83.
- Saito, T., Kimura, S., Nishiyama, Y., & Isogai, A. (2007). Cellulose nanofibers prepared by TEMPO-mediated oxidation of native cellulose. *Biomacromolecules*, 8(8), 2485–2491.
- Saito, T., Kuramae, R., Wohler, J., Berglund, L. A., & Isogai, A. (2013). An ultralong nanofibrillar material: The strength of single cellulose nanofibrils revealed via sonication-induced fragmentation. *Biomacromolecules*, 14(1), 248–253.
- Saito, T., Nishiyama, Y., Putaux, J.-L., Vignon, M., & Isogai, A. (2006). Homogeneous suspensions of individualized microfibrils from TEMPO-catalyzed oxidation of native cellulose. *Biomacromolecules*, 7(6), 1687–1691.
- Sayers, C. M., & den Boer, L. D. (2016). The elastic anisotropy of clay minerals. *Geophysics*, 81(5), C193–C203.
- Sehaqui, H., Liu, A., Zhou, Q., & Berglund, L. A. (2010). Fast preparation procedure for large, flat cellulose and cellulose/inorganic nanopaper structures. *Biomacromolecules*, 11(9), 2195–2198.
- Šturcová, A., Davies, G. R., & Eichhorn, S. J. (2005). Elastic modulus and stress-transfer properties of tunicate cellulose whiskers. *Biomacromolecules*, 6(2), 1055–1061.
- Tang, Z., Kotov, N. A., Magonov, S., & Ozturk, B. (2003). Nanostructured artificial nacre. *Nature Materials*, 2(6), 413–418.
- Tanpichai, S., Quero, F., Nogi, M., Yano, H., Young, R. J., Lindström, T., & Eichhorn, S. J. (2012). Effective Young’s modulus of bacterial and microfibrillated cellulose fibrils in fibrous networks. *Biomacromolecules*, 13(5), 1340–1349.
- Walther, A., Bjuhager, L., Malho, J.-M., Pere, J., Ruokolainen, J., Berglund, L. A., & Ikkala, O. (2010). Large-area, lightweight and thick biomimetic composites with superior material properties via fast, economic, and green pathways. *Nano Letters*, 10(8), 2742–2748.
- Walther, A., Bjuhager, L., Malho, J.-M., Ruokolainen, J., Berglund, L., & Ikkala, O. (2010). Supramolecular control of stiffness and strength in lightweight high-performance nacre-mimetic paper with fire-shielding properties. *Angewandte Chemie International Edition*, 49(36), 6448–6453.
- Wang, J., Cheng, Q., Lin, L., Chen, L., & Jiang, L. (2013). Understanding the relationship of performance with nanofiller content in the biomimetic layered nanocomposites. *Nanoscale*, 5(14), 6356–6362.
- Wang, J., Cheng, Q., Lin, L., & Jiang, L. (2014). Synergistic toughening of bioinspired poly(vinyl alcohol)–clay–nanofibrillar cellulose artificial nacre. *ACS Nano*, 8(3), 2739–2745.
- Wang, Y., Wohler, J., Berglund, L. A., Tu, Y., & Ågren, H. (2014). Molecular dynamics simulation of strong interaction mechanisms at wet interfaces in clay–polysaccharide nanocomposites. *Journal of Materials Chemistry A*, 2(25), 9541–9547.
- Wohler, J., Bergenstråhle-Wohler, M., & Berglund, L. A. (2012). Deformation of cellulose nanocrystals: Entropy, internal energy and temperature dependence. *Cellulose*, 19(6), 1821–1836.
- Wu, C. N., Saito, T., Fujisawa, S., Fukuzumi, H., & Isogai, A. (2012). Ultrastrong and high gas-barrier nanocellulose/clay-layered composites. *Biomacromolecules*, 13(6), 1927–1932.
- Wu, C. N., Yang, Q., Takeuchi, M., Saito, T., & Isogai, A. (2014). Highly tough and transparent layered composites of nanocellulose and synthetic silicate. *Nanoscale*, 6(1), 392–399.
- Xu, D., Wang, S., Berglund, L. A., & Zhou, Q. (2021). Surface charges control the structure and properties of layered nanocomposite of cellulose nanofibrils and clay platelets. *ACS Applied Materials & Interfaces*, 13(3), 4463–4472.
- Yang, M., Hou, Y., & Kotov, N. A. (2012). Graphene-based multilayers: Critical evaluation of materials assembly techniques. *Nano Today*, 7(5), 430–447.
- Yang, X., Jungstedt, E., Reid, M. S., & Berglund, L. A. (2021). Polymer films from cellulose nanofibrils—Effects from interfacial interphase on mechanical behavior. *Macromolecules*, 54(9), 4443–4452.
- Yang, X., Reid, M. S., Olsen, P., & Berglund, L. A. (2020). Eco-friendly cellulose nanofibrils designed by nature: Effects from preserving native state. *ACS Nano*, 14(1), 724–735.

- Yao, K., Huang, S., Tang, H., Xu, Y., Buntkowsky, G., Berglund, L. A., & Zhou, Q. (2017). Bioinspired interface engineering for moisture resistance in nacre-mimetic cellulose nanofibrils/clay nanocomposites. *ACS Applied Materials & Interfaces*, *9*(23), 20169–20178.
- Zerda, A. S., & Lesser, A. J. (2001). Intercalated clay nanocomposites: Morphology, mechanics, and fracture behavior. *Journal of Polymer Science Part B: Polymer Physics*, *39*(11), 1137–1146.
- Zhao, C., Zhang, P., Zhou, J., Qi, S., Yamauchi, Y., Shi, R., & Liu, M. (2020). Layered nanocomposites by shear-flow-induced alignment of nanosheets. *Nature*, *580*(7802), 210–215.
- Zhou, Y., Ono, Y., Takeuchi, M., & Isogai, A. (2020). Changes to the contour length, molecular chain length, and solid-state structures of nanocellulose resulting from sonication in water. *Biomacromolecules*, *21*(6), 2346–2355.